NANO LETTERS

Letter

pubs.acs.org/NanoLett

Ultrafast Nanoimaging of the Photoinduced Phase Transition Dynamics in VO_2

Sven A. Dönges,[†] Omar Khatib,[†] Brian T. O'Callahan,[†] Joanna M. Atkin,[‡] Jae Hyung Park,[§] David Cobden,[§] and Markus B. Raschke*[,†]

[†]Department of Physics, Department of Chemistry, and JILA, University of Colorado, Boulder, Colorado 80309, United States

[‡]Department of Chemistry, University of North Carolina, Chapel Hill, North Carolina 27514, United States

[§]Department of Physics, University of Washington, Seattle, Washington 98195, United States

Supporting Information

ABSTRACT: Many phase transitions in correlated matter exhibit spatial inhomogeneities with expected yet unexplored effects on the associated ultrafast dynamics. Here we demonstrate the combination of ultrafast nondegenerate pump−probe spectroscopy with far from equilibrium excitation, and scattering scanning near-field optical microscopy (*s*-SNOM) for ultrafast nanoimaging. In a femtosecond near-field near-IR (NIR) pump and mid-IR (MIR) probe study, we investigate the photoinduced insulator-to-metal (IMT) transition in nominally homogeneous VO_2 microcrystals. With pump fluences as high as 5 mJ/cm^2, we can reach three distinct excitation regimes. We observe a spatial heterogeneity on ∼50−100 nm length scales in the fluence-dependent IMT dynamics ranging from <100 fs to ∼1 ps. These results suggest a high sensitivity of the IMT with respect to small local variations in strain, doping, or defects that are difficult to discern microscopically. We provide a perspective with the distinct requirements and considerations of ultrafast spatiotemporal nanoimaging of phase transitions in quantum materials.

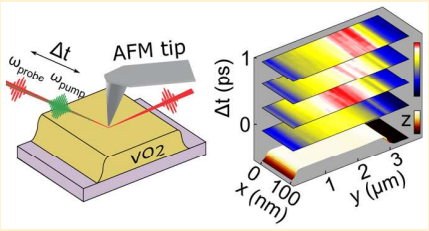

KEYWORDS: *Nano-imaging, ultrafast spectroscopy, vanadium dioxide, s-SNOM, phase transition*

Ultrafast pump−probe spectroscopy provides access to the coupled degrees of freedom of spin, charge, and lattice dynamics that underly the complex properties of many-body systems and correlated quantum materials.[1−3] In order to simultaneously probe the intrinsic and extrinsic heterogeneities associated with these often competing interactions, significant advances have recently been made in combining ultrafast electron, X-ray, and optical spectroscopies with different microscopy techniques toward spatiotemporal imaging.[4−6]

The combination of broadband and ultrafast laser sources with scanning probes, notably scattering scanning near-field optical microscopy (*s*-SNOM), has recently allowed for ultrafast near-field imaging of both coherent[7−9] and incoherent[10,11] dynamics on the nanoscale in conjunction with advances in ultrafast scanning tunneling microscopy.[12,13] However, with these experiments performed in the weak perturbation regime the extension to pump−probe nanospectroscopy for the investigation of spatiotemporal dynamics with high fluence excitation has become desirable.

Here we demonstrate ultrafast nondegenerate pump−probe nanoimaging of the photoinduced femtosecond to picosecond insulator-to-metal (IMT) transition dynamics of vanadium dioxide (VO_2). The IMT in this prototypical correlated electron material can be induced both thermally (T_{IMT} ∼ 340 K)[2,14] and optically,[15,16] but the complex coupling between the structural and electronic degrees of freedom is yet to be fully understood.[17−19] In many previous studies, focusing on polycrystalline thin films created difficulties in accessing the intrinsic material response.[20−22] Yet, microscale pump−probe spectroscopy revealed further heterogeneities with large variability in the IMT dynamics even among well-defined single crystals.[17]

In this work, we perform spatiotemporal nanoimaging of the photoinduced IMT dynamics in VO_2 microcrystals, ranging from a weakly perturbing hot carrier excitation up to a fully saturated phase transition. Most notably we register for a particular pump fluence the presence of the different dynamical regimes on the same crystal within just a few 100 nm spatial separation. The results are indicative of a high sensitivity of the IMT to defects and impurities, possibly affecting the local electronic structure through strain and doping, even within nominally homogeneous VO_2 microcrystals. The example of VO_2 demonstrates the applicability of ultrafast pump−probe *s*-SNOM for the investigation of nanoscale heterogeneities in the phase transition behavior of correlated matter.

Experiment. Figure 1a shows a schematic of our near-field pump−probe experiment. Near-infrared (NIR) pump pulses are provided by a Yb-doped tungstate oscillator/amplifier (Yb:KGW, Pharos, Light Conversion) with center wavelength λ = 1032 nm and pulse duration of τ_{NIR} = 190 ± 5 fs with flat

Received: December 30, 2015
Revised: April 5, 2016
Published: April 20, 2016

DOI: 10.1021/acs.nanolett.5b05313
Nano Lett. 2016, 16, 3029−3035

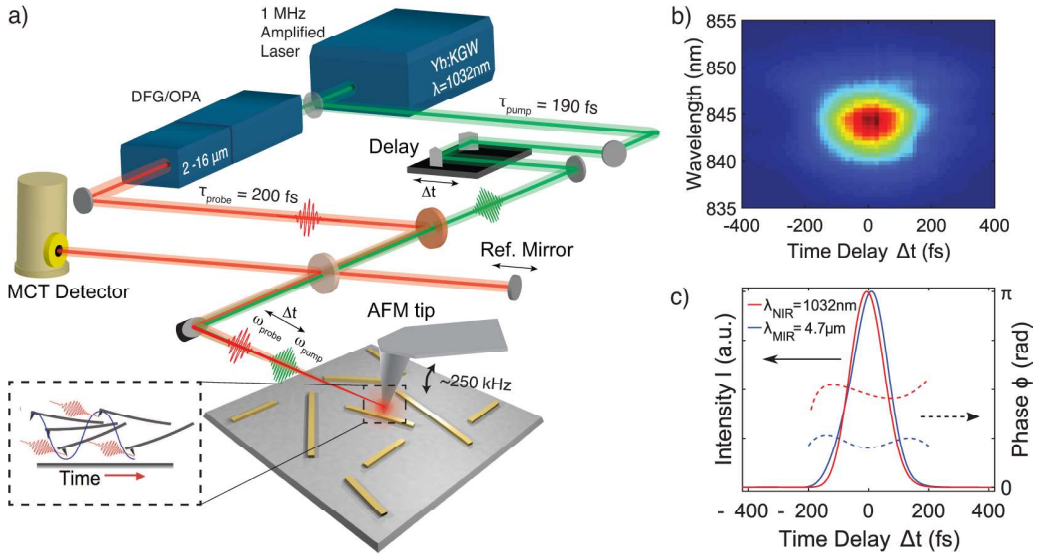

Figure 1. (a) Optical layout with amplified laser system providing 190 fs NIR (1032 nm) pump pulses and widely tunable (2−16 μm) 200 fs MIR probe pulses that are collinearly focused onto the *s*-SNOM/AFM tip with the scattered near-field probe response detected with homo- or heterodyne optical amplification. Inset: laser-tip interaction with few pulses per tip oscillation. (b) Typical X-FROG spectrogram of the probe pulse with (c) full phase and intensity transient reconstruction, characterizing pulse durations of ~200 fs for both the NIR pump and MIR probe pulses at the tip apex.

spectral phase as determined by frequency resolved optical gating (FROG). Tunable mid-infrared (MIR) probe light is generated via optical parametric amplification and difference frequency generation with tuning range from 2−16 μm. Pump and probe beam are recombined collinearly using an antireflection coated Ge beam combiner, then focused onto the tip apex of a modified atomic force microscope (attoAFM I, Attocube Systems AG) with polarization parallel to the tip axis, using an off-axis parabolic mirror (focal length f = 11.25 mm, numerical aperture NA = 0.45).[23] For near-field signal enhancement, commercial silicon tips with a PtIr coating and a resonance frequency of 250 ± 20 kHz (ARROW-NCPt, NanoWorld) are used. The laser system operating at variable repetition rate ~0.9−1 MHz can be synchronized to a harmonic frequency of the cantilever motion ($n\omega_{tip}$) in noncontact mode with typically n = 4 (Figure 1a inset). The signal is detected with a mercury−cadmium−telluride (MCT) detector (KLD-0.1,Kolmar) with residual pump light blocked by a Ge filter. Using a digital lock-in amplifier (HF2LI, Zurich Instruments) the signal is demodulated at a higher harmonic of the tip tapping frequency $m\omega_{tip}$ (m = 2, 3) to distinguish between far-field and near-field contributions to the overall signal, as is well established in *s*-SNOM for near-field discrimination.[24,25] As a compromise between signal intensity and isolating the near-field interaction, our *s*-SNOM signal is optimized and detected at $2\omega_{tip}$.[26]

A variable NIR pump fluence of nominally up to 5 mJ/cm^2 (see Supporting Information) and limited by tip damage is applied for excitation of VO_2. We split off a fraction of the amplified fundamental wavelength λ_{NIR} = 1032 nm (1.2 eV) as our pump, which provides above bandgap (~0.67 eV in VO_2) excitation to photoinduce the IMT. The MIR probe parameters with center wavelength λ_{MIR} = 4.7 μm ($\Delta\lambda_{fwhm}$ = 0.2 μm) and fluence of 100 μJ/cm^2 are set to maximize the *s*-SNOM signal and access the free carrier response of the metallic phase of VO_2, while still being nonperturbative. The MIR probe pulse duration at the tip is determined by sum-frequency cross-correlation FROG (X-FROG, Figure 1b) with derived intensity transient $E^2_{MIR}(\Delta t)$ and temporal phase $\phi(\Delta t)$ shown in Figure 1c, corresponding to a pulse duration τ_{MIR} = 200 ± 10 fs.

Pump−probe *s*-SNOM traces are recorded as a function of the time delay between pump and probe pulses as in conventional ultrafast optical spectroscopy but with *s*-SNOM spatial resolution limited only by the radius of the tip apex, typically 10−20 nm.[27] The *s*-SNOM probe wavelength λ_{MIR} = 4.7 μm measures the tail of the Drude response to probe the pump-induced metallic phase (Figure 2d), without interference from any lattice or other electronic excitations.[28,29] The pump−probe *s*-SNOM signal is acquired with self-homodyne detection,[30] where the tip-scattered near-field is amplified by

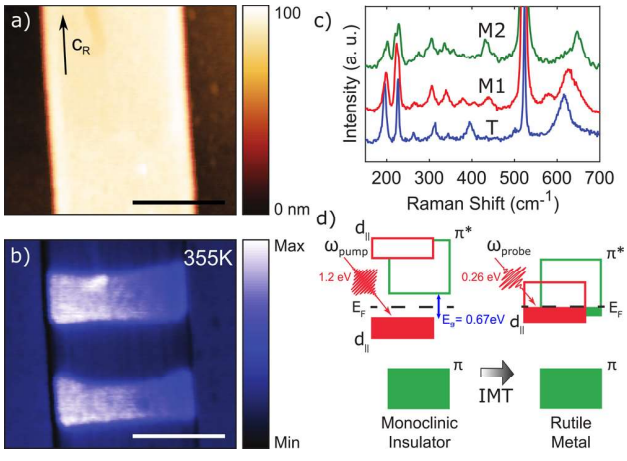

Figure 2. (a) Topography and (b) IR *s*-SNOM image of a typical VO_2 microcrystal with (b) showing coexistence of insulating (low signal, dark areas) and metallic (high signal, bright areas) phases when heated to 355 K (scale bar 1 μm). (c) Representative Raman traces of the different structural phases occurring upon heating VO_2 microcrystals through the IMT. The mode at ~520 cm^{-1} is from the Si substrate phonon. (d) Schematic of the electronic band structure of VO_2 indicating the difference between the insulating and metallic phases.

DOI: 10.1021/acs.nanolett.5b05313
Nano Lett. 2016, 16, 3029−3035

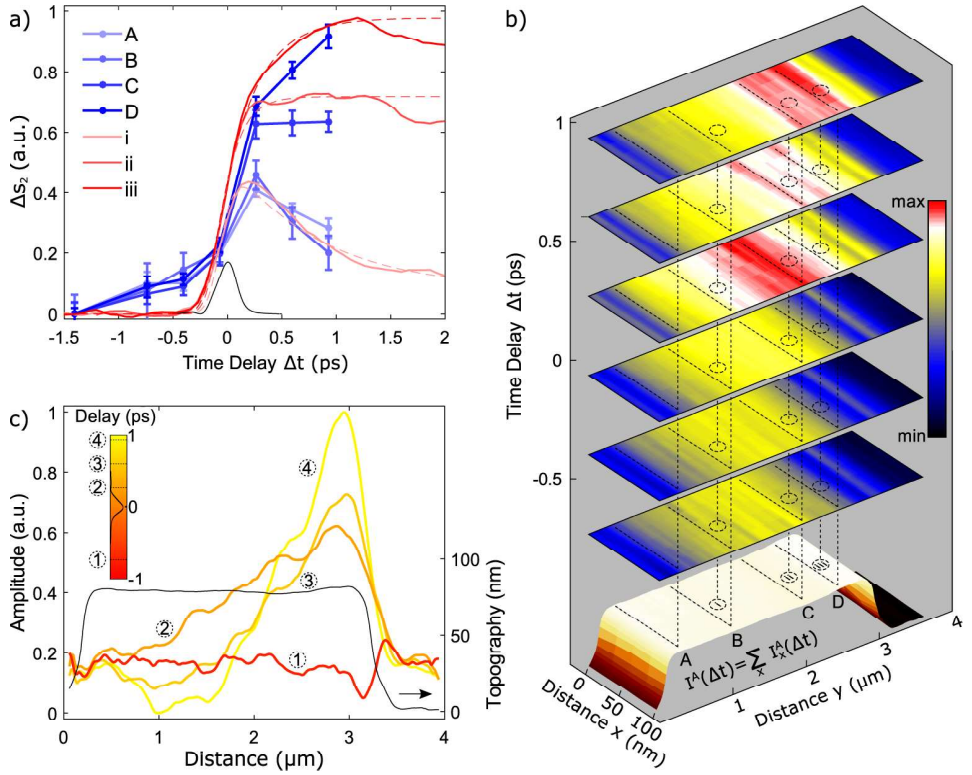

Figure 3. (a) Near-field pump–probe time traces recorded on different positions on a microcrystal (red, positions indicated in panel b), together with full time traces extracted from a series of spatiotemporal images (blue, images and positions shown in panel b). (b) Set of images showing spatial and temporal variations in the IMT dynamics of a single VO_2 microcrystal. (c) Line profiles for several pump–probe time delays across the microcrystal shown in panel b.

a local background reference field (see Supporting Information for details). We define a relative near-field amplitude Δs_2, where the subscript denotes demodulation at $2\omega_{tip}$, corresponding to the pump induced signal change normalized to the maximum signal difference between the insulating and metallic phase.

Results. We use vapor transport-grown VO_2 single domain microcrystals, as described previously.[31−33] For precharacterization, Figure 2 shows AFM topography (a) together with continuous wave IR *s*-SNOM at 10.6 μm (b) obtained on a flat VO_2 microcrystal when heated to 355 K, where areas of high (bright) and low (dark) signal in Figure 2b reflect alternating metallic and insulating domains. This nanoscale metallic domain formation perpendicular to the crystallographic *c*-axis (c_R) is known to be due to the strain introduced by different coefficients of thermal expansion between VO_2 and the Si substrate, as has been established previously.[32,33]

Additionally, to explore the different possible structural phases of VO_2 coexisting in the insulating microcrystals, we perform temperature-dependent micro-Raman spectroscopy using HeNe laser excitation at λ = 632 nm. Figure 2c shows representative Raman spectra of the different insulating structural phases: M1, M2, and triclinic, as the microcrystals are heated through the IMT. In agreement with studies of the temperature-strain phase diagram of VO_2,[27,34] the crystals transition between the different insulating phases in a well-defined and repeatable fashion.[27]

Figure 2d shows a schematic of the difference in the electronic band structure of VO_2 between the equilibrium insulating and metallic states. In the monoclinic M1 phase, it is conventionally understood that dimerization of the vanadium ions splits the $d_{||}$ orbitals into bonding and antibonding states, opening up a bandgap (~0.67 eV).[35] Through mechanisms still not fully understood, optical pump pulses lead to a collapse of the electronic bandgap on femtosecond time scales, resulting in a finite density of states at the Fermi level, and a free carrier Drude response. Though ultimately arriving at a final metallic state similar to the thermally induced IMT, there could be equally different energetic pathways that govern the ultrafast photoinduced transition that may be equally sensitive to local properties of VO_2.

Figure 3 summarizes our main results for a VO_2 microcrystal, where we observe a range of IMT dynamics in the ultrafast *s*-SNOM traces for various positions on the sample. Figure 3a shows three representative yet distinct pump–probe transients observed on the same microcrystal in close proximity to each other (i, ii, and iii), and all acquired for the same nominal pump fluence of 2.9 mJ/cm^2. The behavior of (i) shows an immediate excitation at time delay Δt = 0 that quickly relaxes back to its initial value. In VO_2 this behavior is representative of photoexcitation below the IMT threshold, followed by free carrier relaxation on ps time scales.[21] In contrast, after the initial rise, traces (ii) and (iii) both show a persistent long-lived elevated signal level where, notably for trace (iii) the initial signal rise is continuous and over an extended period before reaching its maximum value at ~1 ps. This trend in the pump–probe time dynamics is characteristic for driving the photo-induced IMT with the emergence of a stable signal level lasting up to several microseconds indicating the metallic phase. Early IMT transition dynamics on time scales $\lesssim$150 fs[16,17,21] appear instantaneous within the time resolution of the experiment.

DOI: 10.1021/acs.nanolett.5b05313
Nano Lett. 2016, 16, 3029–3035

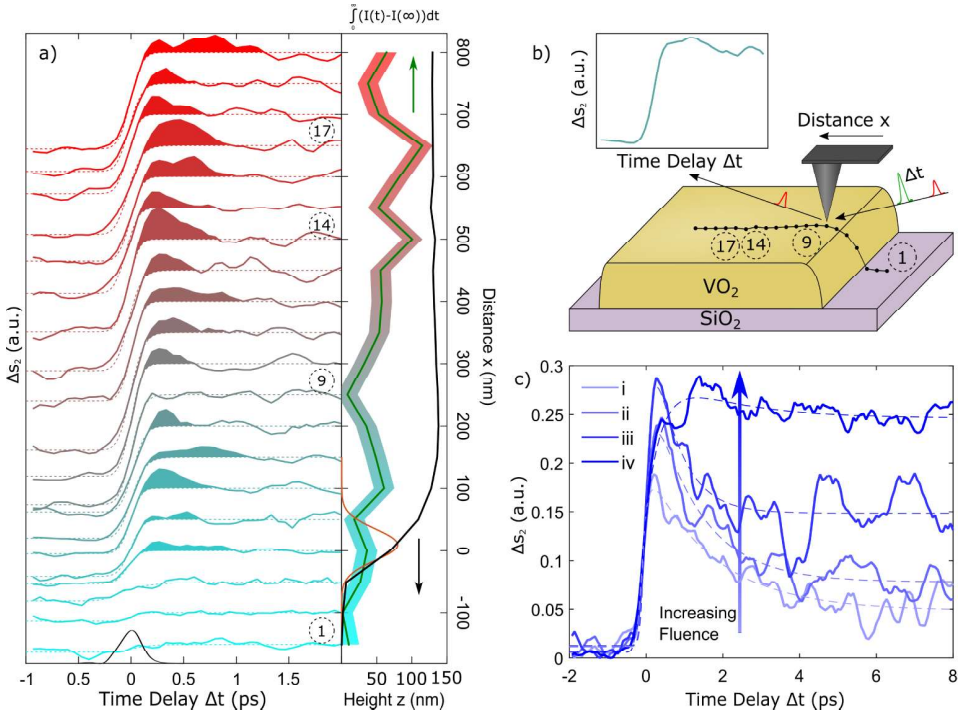

Figure 4. (a) Near-field pump−probe time traces recorded at 50 nm intervals while moving onto a VO_2 microcrystal as illustrated in (b). Shaded areas in the left panel and the curve in the right panel of a are a measure of the degree of the photoinduced IMT, compared to a fit to the long-time behavior as described in the text. (c) Fluence-dependent time traces on a VO_2 microcrystal showing different regimes of photoinduced transition through the IMT.

However, the slower rise of the signal level to its peak value as resolved in transient (iii) is consistent with a longer IMT transition time and signal increase for higher pump fluences, as also observed recently in far-field degenerate pump−probe experiments.[17]

To further investigate the spatial inhomogeneities in the ultrafast dynamics, Figure 3b shows *s*-SNOM images across the VO_2 microcrystal taken at different time delays. The emergence of the pump-induced metallic phase shows both spatial and temporal variations. Interestingly, the data exhibit an intermediate signal decrease between $\tau \sim 0.3$ ps and $\tau = 0.6$ ps before rising again at $\tau \sim 0.9$ ps. Notably, the images show that the location of maximum signal on the microcrystal shifts from close to the center of the crystal toward the edge at later times. This behavior is further illustrated in Figure 3a. Four time traces (blue, A−D) were extracted from the spatial scans at different locations on the microcrystal as indicated, representing the spatially varying pump−probe dynamics across the width of the rod. On the left side of the rod (A,B), only an initial electronic excitation that quickly relaxes is seen. In contrast, toward the right edge of the microcrystal the system is locally driven through the photoinduced IMT (C). This local IMT behavior is even more pronounced for position D, where the continuing increase in IMT signal level for larger time delays τ indicates the increased transiton rise time as mentioned above.

Figure 3c shows near-field pump−probe intensity line cuts across the same microcrystal for selected temporal snapshots, and illustrates the much higher IMT signal on the right side of the crystal at $\tau \sim 0.9$ ps compared to shorter time delays. The profiles are averaged over the long crystal axis (x direction) as indicated in Figure 3b and normalized to the unpumped crystal at $\tau \sim -1.4$ ps. For most of the width of the microcrystal, the signal in profile 2 is strongest because of the dominance of the free carrier response after the initial electronic excitation. The continuous signal rise on the right third of the microcrystal is indicative of the photoinduced IMT in that region compared to the relaxation of the free carrier response on the left side (profile 4). For additional insight into the local spatial variations of the IMT dynamics on VO_2 microcrystals, Figure 4a shows a linear series of pump−probe time traces taken at 50 nm increments across the edge of a different microcrystal with a schematic of the experimental procedure shown in Figure 4b. Individual time traces have been vertically offset to symbolize their position with respect to the VO_2 microcrystal edge, shown in the right panel of Figure 4a. We observe that across the crystal the response to the incident pump light is far from spatially homogeneous with a large variation between a fully photoinduced phase transition (trace 9) and an initial electronic excitation quickly decaying into a metastable state (most prominent in traces 14 and 17). The degree of these variations is visualized by plotting the integrated difference between the data and a long time fit to the data (details below), where a small integral response is indicative of a fully photoinduced phase transition and a large integral shows subthreshold areas of the microcrystal where relaxation occurs. In contrast to the variations between time traces as displayed in Figures 3 and 4a, Figure 4c shows fluence-dependent variations in the pump−probe response for fluences between 4.1 (light blue) and 4.7 mJ/cm^2 (dark blue) at a fixed location.

The dashed lines in Figures 3a and 4c are fits to the respective *s*-SNOM time traces assuming a response function of the microcrystal described by

DOI: 10.1021/acs.nanolett.5b05313
Nano Lett. 2016, 16, 3029−3035

$$\Delta s_2(t) = A_{bg} + \Theta(t - t_0) \left\{ A_R \exp\left(-\frac{t - t_0}{\tau_R}\right) + A_D\left(\exp\left(-\frac{t - t_0}{\tau_D}\right) - 1\right)\right\} \quad (1)$$

where $\Theta(t - t_0)$ is the Heaviside step function. A_{bg}, A_R, and A_D are a flat background, the amplitude of the signal rise, and decay amplitude, respectively. τ_R and τ_D describe the corresponding time constants of rise and decay, respectively. $\Delta s_2(t)$ is convolved with the *s*-SNOM setup response function, with pump and probe transients retrieved from the FROG and X-FROG traces, respectively (see Figure 1b,c). For signal traces (ii) and (iii) in Figure 3a, the amplitude of the decay was manually fixed to $A_D = 0$ to avoid fitting artifacts. The fit results are summarized in Table 1. The signal rise to a constant flat

Table 1. Fit Results of VO_2 *s*-SNOM Pump–Probe Transients with an Estimated Uncertainty of ±30 fs for τ_R and ±100 fs for τ_D for Fluence Regimes Ranging from below-Threshold Hot Carrier Relaxation to near and above Threshold IMT

					photoinduced IMT		
VO_2 response	hot carrier relaxation				near threshold	above threshold	
Trace (Figure)	3(i)	4(i)	4(ii)	4(iii)	3(ii)	3(iii)	4(iv)
τ_R (fs)	<100	110	140	150	140	310	410
τ_D (ps)	0.9	1.8	1.2	0.7	>10	>10	>10

infrared probe response after initial photoexcitation indicates a fully driven IMT and persistent metallic state for up to several microseconds. In contrast, a fast decay within a few picoseconds to either a metastable intermediate signal level or the base signal level implies below threshold electronic excitation. For time traces (i)–(iii) in Figure 3a we find an increase in rise time τ_R from less than 100 fs (limited by the temporal resolution of the experiment) for trace (i) to $\tau_R^{(iii)}$ = 310 fs for trace (iii), with an estimated uncertainty in the fits of ±30 fs (see Table 1). This observation is in qualitative agreement with a previously found 3-fold increase in the ultrafast photoinduced transition time with increasing pump fluence.[17] Similarly, the fits in Figure 4c show qualitatively the same VO_2 behavior as in Figure 3a. For the lowest three traces the signal rise time is the same (110, 150, and 140 fs) within an estimated uncertainty of ±30 fs. For the fourth trace, which shows a fully photoinduced IMT, the rise time was calculated to be about three times as high at 400 ± 30 fs. The decay time τ_D was found to decrease with increasing fluence from almost 2 ps to 700 fs with an estimated uncertainty of ±100 fs.

Discussion. In the following, we discuss our observations of the nanoscale spatiotemporal dynamics of the IMT in VO_2 microcrystals in the context of earlier macroscopic time-resolved studies.

The electronic insulator-to-metal transition in VO_2 is characterized by a concomitant structural transition from a monoclinic insulator to a rutile metal phase with suggestions that it exhibits aspects of both electron–lattice (Peierls) and electron–electron (Mott) interactions. The associated complexity in isolating the intrinsic driving mechanism has motivated a range of ultrafast experiments attempting to separate the different electronic and lattice degrees of freedom from time-resolved terahertz (THz) to X-ray and electron diffraction studies.[16,19,20,22,36]

Recent THz[37] and optical[21] pump–probe studies track the coherent phonon oscillations while simultaneously monitoring the electronic response, revealing the importance of the nonequilibrium lattice rearrangement in conjunction with the dynamical changes to the electronic band structure. For example, the loss of insulating phase (M1) phonon modes before the formation of a metallic state[21] could suggest a Peierls-type driving process. On the other hand, there is also recent evidence in ultrafast electron diffraction experiments of a metastable intermediate monoclinic metallic state, where a metal-like free carrier IR response persists with the periodic lattice distortion of the monoclinic M1 phase still intact.[19] Thus, competing interactions and correlations dictate the excited state dynamics and are likely further obscured in studies of granular samples that only allow probing of an ensemble response.

To avoid spatial averaging over the extrinsic heterogeneities associated with polycrystalline thin film samples, single VO_2 micro- or bulk crystals have seen increased usage.[18,32,38,39] However, our recent work on individual VO_2 microcrystals demonstrated even in these systems a large inhomogeneity in the ultrafast transition dynamics with crystal-to-crystal variations that appear uncorrelated with size, temperature, or macroscopic strain.[17] The combination of the results to date suggests a high sensitivity of the IMT in VO_2 in terms of transition temperature, threshold fluence, or dynamical response, with respect to microscopic local variations in, for example, doping, defects, or strain.

Our results shown in Figures 3 and 4 are generally consistent with previous ultrafast far-field studies of VO_2, which indicated three distinct fluence regimes (hot carrier relaxation to an initial or metastable state, the photoinduced IMT, and extended photoexcitation of the IMT above threshold) in the ultrafast transition dynamics,[17,21,22] yet indicate a high degree of spatial heterogeneity in the fluence dependence. Most notable in our experiments is the appearance of these distinct fluence regimes within just a few 100 nm spatial separation for even a nominally identical and constant pump fluence on the individual single crystal level, as clearly seen in Figure 3. This suggests a local variation of the threshold fluence required to photoinduce the IMT which is reinforced by the overall increase in signal level difference after temporal overlap Δt_0, as seen in our fluence-dependent measurements (Figure 4c) and previously on both thin films as well as microcrystals for above threshold excitation.[17,21]

Varying IMT characteristics between microcrystals has previously been attributed to different amounts of strain, defects, and doping.[17,27,32,34,40] From conventional temperature-dependent continuous wave *s*-SNOM experiments, strain between the sample substrate and the VO_2 microcrystals is known to cause domain formation preferentially perpendicular with respect to the *c*-axis (see Figure 2b). In contrast, our spatially resolved pump–probe near-field measurements show an ultrafast transient domain formation parallel to the *c*-axis of the microcrystal, thus suggesting a different manifestation and sensitivity of the ultrafast versus thermal IMT with respect to the inhomogeneities. Specifically, because the structural phase transition does not occur on the time scales of our experiment, this suggests that while domain formation in microcrystals during the thermally induced IMT is governed by the lattice, the electronic degrees of freedom likely dictate the dynamics

DOI: 10.1021/acs.nanolett.5b05313
Nano Lett. 2016, 16, 3029–3035

and spatial variations seen in the ultrafast transition. Random defects are unlikely to be the cause of the observed inhomogeneities, as we would expect them to be distributed equally across the microcrystal. Instead, we believe that slight changes in the oxygen or vanadium concentration and associated defects during the growth process can cause zoning with small variations in the doping or exact stoichiometry of the microcrystal. The resulting spatial variations in the electronic structure are then observed with our high sensitivity to local dynamics causing transient intracrystal domain formation.

With the application to VO_2 as an example, we have demonstrated a new regime of ultrafast pump−probe nanoimaging. Specifically, the use of an amplified pulsed laser source has enabled us to access the dynamics of a highly perturbed excited state of a strongly correlated material. However, for further developing the technique, there are important aspects of ultrafast spectroscopy and imaging in near-field implementations that require critical considerations compared to conventional ultrafast far-field spectroscopy.

In contrast to conventional optical pump−probe experiments, where far-field reflection, transmission, or absorption from the sample is measured directly, the observable in ultrafast *s*-SNOM is a coupled tip−sample polarization response of the probe pulse. The sample response in the form of, for example, dielectric function or optical conductivity is then contained in the complex scattering signal of the near-field interaction $|s|e^{i\phi}$, where s and ϕ are the near-field scattering amplitude and phase, respectively.[41] Several techniques as established in conventional *s*-SNOM[7,8,42] can also be readily applied to the ultrafast regime to directly relate the probe near-field signal to the sample dielectric properties and their pump-induced modification. A self-homodyne measurement, as in our work, involves amplification of the near-field signal by the far-field background with an uncontrolled phase. While already sufficient in simple cases such as a Drude response with a flat spectral phase, the approach can be extended to probe other resonant interaction dynamics as well.[43] In contrast to continuous wave measurements, a pump-induced transient background variation requires possible careful consideration,[11] as detailed in the Supporting Information. With further refinements, the technique can be generalized to probe any resonant electronic, spin, or lattice excitation to obtain the complete transient optical response function by performing coherent, nonlinear, and other phase-resolved measurements using interferometric homo- and heterodyne signal amplification methods.

Despite advantages of the wavelength-independent localization of scattering-based near-field nanoimaging, complications arise in pump−probe *s*-SNOM in terms of quantifying the local pump fluence and thus the strength of the pump perturbation. This problem is associated with the general difficulty of determining the degree of local field enhancement in the tip−sample gap, which can sensitively depend on tip geometry and associated antenna resonances, tip−sample distance, and both tip and sample material.[44] For our specific case of a PtIr tip with 20 nm apex radius and 1032 nm pump wavelength, where only a modest field enhancement of 2−5 can be expected,[44,45] this effect needs careful consideration when more quantitative pump-fluence information is desired.

On the other hand, the tip enhancement offers an avenue to reach pump fluence levels not readily achievable in far-field excitation when combined with optical antenna, metamaterial, and plasmonic resonances on a tip.[46] This might prove partially beneficial for IR or THz pumping, where weak sources and long wavelengths limit achievable fluences in far-field focusing. This could extend THz field-induced phase transitions[47,48] or mode-selective phonon excitation of novel quantum phases[3,49] to the nanoscale.

With fluence levels of 2−5 mJ/cm^2 at the 1032 nm pump wavelength and 200 fs pulse duration, corresponding to a peak field strength of 4−7 MV/cm, this is already close to the damage threshold for the PtIr tips used, and leads to gradual tip degradation. Significantly larger pump fields can be achieved with shorter pulse duration but call for novel tip designs with higher damage thresholds based on refractory metals, conductive oxides, or carbides. This, together with a tuned pulse repetition rate, pulse sequence schemes, or different synchronization techniques with the dynamic cantilever motion opens a new exploratory parameter space for new ultrafast nanoimaging science.

Conclusion. In summary, we have explored near-field pump−probe *s*-SNOM for nanoimaging of a strongly fluence-dependent phase transition. With the example of the photo-induced insulator-to-metal transition in VO_2, we spatially resolve nanoscale subdomain heterogeneity in the far from equilibrium excitation dynamics, with distinct fluence regimes in the same microcrystal within few 100 nm spatial separation. Most notably we observe an ultrafast transient domain formation with orientation fundamentally distinct from the static equilibrium domain texture. This suggests that the photoinduced IMT is highly sensitive with respect to local perturbations in electronic structure through defects or doping-induced during crystal growth. The ability to resolve nanoscale variations in the ultrafast phase transition dynamics may lead the way to assessing the intrinsic IMT mechanisms in VO_2 and possibly other correlated materials. The combination of *s*-SNOM and pump−probe spectroscopy with high fluence excitation opens a new regime of spatiotemporal nanoimaging.

■ ASSOCIATED CONTENT

Supporting Information

The Supporting Information is available free of charge on the ACS Publications website at DOI: 10.1021/acs.nanolett.5b05313.

Pump fluence estimation; Pump−probe sample volume; self-homodyne pump−probe *s*-SNOM. (PDF)

■ AUTHOR INFORMATION

Author Contributions

S.A.D. and O.K. contributed equally to this work. M.B.R., S.A.D., J.M.A., and O.K. conceived the experiment. J.H.P. and D.C. prepared the samples. S.A.D. and O.K. performed the ultrafast and nanoimaging measurements and analyzed the data. B.T.O. performed thermal and Raman measurements. S.A.D., O.K., and M.B.R. wrote the manuscript with contributions from J.M.A. All authors discussed the results and commented on the manuscript. M.B.R. supervised the project.

Notes

The authors declare no competing financial interest.

■ ACKNOWLEDGMENTS

The authors would like to thank Aaron Sternbach, Alex McLeod, and Dimitri Basov for stimulating discussions. Funding was provided by the U.S. Department of Energy, Office of Basic Sciences, Division of Material Sciences and Engineering, under Award No. DE-SC0008807.

DOI: 10.1021/acs.nanolett.5b05313
Nano Lett. 2016, 16, 3029−3035

REFERENCES

(1) Basov, D. N.; Averitt, R. D.; van der Marel, D.; Dressel, M.; Haule, K. *Rev. Mod. Phys.* **2011**, *83*, 471−541.
(2) Imada, M.; Fujimori, A.; Tokura, Y. *Rev. Mod. Phys.* **1998**, *70*, 1039−1263.
(3) Rini, M.; Tobey, R.; Dean, N.; Itatani, J.; Tomioka, Y.; Tokura, Y.; Schoenlein, R. W.; Cavalleri, A. *Nature* **2007**, *449*, 72−74.
(4) Zewail, A. H. *Science* **2010**, *328*, 187−193.
(5) Gaffney, K. J.; Chapman, H. N. *Science* **2007**, *316*, 1444−1448.
(6) Wagner, M.; et al. *Nano Lett.* **2014**, *14*, 894−900.
(7) Xu, X. G.; Raschke, M. B. *Nano Lett.* **2013**, *13*, 1588−1595.
(8) Atkin, J. M.; Sass, P. M.; Teichen, P. E.; Eaves, J. D.; Raschke, M. B. *J. Phys. Chem. Lett.* **2015**, *6*, 4616−4621.
(9) Guenther, T.; Lienau, C.; Elsaesser, T.; Glanemann, M.; Axt, V. M.; Kuhn, T.; Eshlaghi, S.; Wieck, A. D. *Phys. Rev. Lett.* **2002**, *89*, 057401.
(10) Wagner, M.; McLeod, A. S.; Maddox, S. J.; Fei, Z.; Liu, M.; Averitt, R. D.; Fogler, M. M.; Bank, S. R.; Keilmann, F.; Basov, D. N. *Nano Lett.* **2014**, *14*, 4529−4534.
(11) Eisele, M.; Cocker, T. L.; Huber, M. A.; Plankl, M.; Viti, L.; Ercolani, D.; Sorba, L.; Vitiello, M. S.; Huber, R. *Nat. Photonics* **2014**, *8*, 841−845.
(12) Terada, Y.; Yoshida, S.; Takeuchi, O.; Shigekawa, H. *Nat. Photonics* **2010**, *4*, 869−874.
(13) Yoshida, S.; Aizawa, Y.; Wang, Z.-h.; Oshima, R.; Mera, Y.; Matsuyama, E.; Oigawa, H.; Takeuchi, O.; Shigekawa, H. *Nat. Nanotechnol.* **2014**, *9*, 588−593.
(14) Morin, F. J. *Phys. Rev. Lett.* **1959**, *3*, 34.
(15) Cavalleri, A.; Tóth, C.; Siders, C. W.; Squier, J. A.; Ráksi, F.; Forget, P.; Kieffer, J. C. *Phys. Rev. Lett.* **2001**, *87*, 237401.
(16) Cavalleri, A.; Dekorsy, T.; Chong, H. H. W.; Kieffer, J. C.; Schoenlein, R. W. *Phys. Rev. B: Condens. Matter Mater. Phys.* **2004**, *70*, 161102.
(17) O'Callahan, B. T.; Jones, A. C.; Hyung Park, J.; Cobden, D. H.; Atkin, J. M.; Raschke, M. B. *Nat. Commun.* **2015**, *6*, 6849.
(18) Liu, M.; et al. *Phys. Rev. B: Condens. Matter Mater. Phys.* **2015**, *91*, 245155.
(19) Morrison, V. R.; Chatelain, R. P.; Tiwari, K. L.; Hendaoui, A.; Bruhács, A.; Chaker, M.; Siwick, B. J. *Science* **2014**, *346*, 445−448.
(20) Wegkamp, D.; Herzog, M.; Xian, L.; Gatti, M.; Cudazzo, P.; McGahan, C. L.; Marvel, R. E.; Haglund, R. F.; Rubio, A.; Wolf, M.; Stähler, J. *Phys. Rev. Lett.* **2014**, *113*, 216401.
(21) Wall, S.; Foglia, L.; Wegkamp, D.; Appavoo, K.; Nag, J.; Haglund, R. F.; Stähler, J.; Wolf, M. *Phys. Rev. B: Condens. Matter Mater. Phys.* **2013**, *87*, 115126.
(22) Cocker, T. L.; Titova, L. V.; Fourmaux, S.; Holloway, G.; Bandulet, H.-C.; Brassard, D.; Kieffer, J.-C.; El Khakani, M. A.; Hegmann, F. A. *Phys. Rev. B: Condens. Matter Mater. Phys.* **2012**, *85*, 155120.
(23) Yang, H. U.; Hebestreit, E.; Josberger, E. E.; Raschke, M. B. *Rev. Sci. Instrum.* **2013**, *84*, 023701.
(24) Keilmann, F.; Hillenbrand, R. *Philos. Trans. R. Soc., A* **2004**, *362*, 787−805.
(25) Atkin, J. M.; Berweger, S.; Jones, A. C.; Raschke, M. B. *Adv. Phys.* **2012**, *61*, 745−842.
(26) Atkin, J. M.; Raschke, M. B. *Nature* **2013**, *498*, 44−45.
(27) Atkin, J. M.; Berweger, S.; Chavez, E. K.; Raschke, M. B.; Cao, J.; Fan, W.; Wu, J. *Phys. Rev. B: Condens. Matter Mater. Phys.* **2012**, *85*, 020101.
(28) Barker, A. S.; Verleur, H. W.; Guggenheim, H. J. *Phys. Rev. Lett.* **1966**, *17*, 1286−1289.
(29) Choi, H. S.; Ahn, J. S.; Jung, J. H.; Noh, T. W.; Kim, D. H. *Phys. Rev. B: Condens. Matter Mater. Phys.* **1996**, *54*, 4621−4628.
(30) Raschke, M. B.; Molina, L.; Elsaesser, T.; Kim, D. H.; Knoll, W.; Hinrichs, K. *ChemPhysChem* **2005**, *6*, 2197−2203.
(31) Guiton, B. S.; Gu, Q.; Prieto, A. L.; Gudiksen, M. S.; Park, H. *J. Am. Chem. Soc.* **2005**, *127*, 498−9.
(32) Jones, A. C.; Berweger, S.; Wei, J.; Cobden, D.; Raschke, M. B. *Nano Lett.* **2010**, *10*, 1574−1581.
(33) Wu, J.; Gu, Q.; Guiton, B.; de Leon, N.; Ouyang, L.; Park, H. *Nano Lett.* **2006**, *6*, 2313−2317.
(34) Park, J. H.; Coy, J. M.; Kasirga, T. S.; Huang, C.; Fei, Z.; Hunter, S.; Cobden, D. H. *Nature* **2013**, *500*, 431−434.
(35) Rini, M.; Hao, Z.; Schoenlein, R. W.; Giannetti, C.; Parmigiani, F.; Fourmaux, S.; Kieffer, J. C.; Fujimori, A.; Onoda, M.; Wall, S.; Cavalleri, A. *Appl. Phys. Lett.* **2008**, *92*, 181904.
(36) Hara, S.; Li, J. *Phys. Rev. B: Condens. Matter Mater. Phys.* **2010**, *82*, 184114.
(37) Kübler, C.; Ehrke, H.; Huber, R.; Lopez, R.; Halabica, A.; Haglund, R. F.; Leitenstorfer, A. *Phys. Rev. Lett.* **2007**, *99*, 116401.
(38) Wei, J.; Wang, Z.; Chen, W.; Cobden, D. H. *Nat. Nanotechnol.* **2009**, *4*, 420−424.
(39) Hu, B.; Ding, Y.; Chen, W.; Kulkarni, D.; Shen, Y.; Tsukruk, V. V.; Wang, Z. L. *Adv. Mater.* **2010**, *22*, 5134−5139.
(40) Marezio, M.; McWhan, D. B.; Remeika, J. P.; Dernier, P. D. *Phys. Rev. B* **1972**, *5*, 2541−2551.
(41) Hillenbrand, R.; Keilmann, F. *Phys. Rev. Lett.* **2000**, *85*, 3029−3032.
(42) Huth, F.; Govyadinov, A.; Amarie, S.; Nuansing, W.; Keilmann, F.; Hillenbrand, R. *Nano Lett.* **2012**, *12*, 3973−3978.
(43) Pollard, B.; Maia, F. C. B.; Raschke, M. B.; Freitas, R. O. *Nano Lett.* **2016**, *16*, 55−61.
(44) Neacsu, C.; Steudle, G.; Raschke, M. *Appl. Phys. B: Lasers Opt.* **2005**, *80*, 295−300.
(45) Thomas, S.; Wachter, G.; Lemell, C.; Burgdörfer, J.; Hommelhoff, P. *New J. Phys.* **2015**, *17*, 063010.
(46) Berweger, S.; Atkin, J. M.; Olmon, R. L.; Raschke, M. B. *J. Phys. Chem. Lett.* **2012**, *3*, 945−952.
(47) Liu, M.; Hwang, H. Y.; Tao, H.; Strikwerda, A. C.; Fan, K.; Keiser, G. R.; Sternbach, A. J.; West, K. G.; Kittiwatanakul, S.; Lu, J.; Wolf, S. A.; Omenetto, F. G.; Zhang, X.; Nelson, K. A.; Averitt, R. D. *Nature* **2012**, *487*, 345−348.
(48) Kampfrath, T.; Tanaka, K.; Nelson, K. A. *Nat. Photonics* **2013**, *7*, 680−690.
(49) Fausti, D.; Tobey, R. I.; Dean, N.; Kaiser, S.; Dienst, A.; Hoffmann, M. C.; Pyon, S.; Takayama, T.; Takagi, H.; Cavalleri, A. *Science* **2011**, *331*, 189−191.

DOI: 10.1021/acs.nanolett.5b05313
Nano Lett. 2016, 16, 3029−3035